New Journal of Physics

The open access journal at the forefront of physics





PAPER • OPEN ACCESS

Binary mixtures of intelligent active Brownian particles with visual perception

To cite this article: Rajendra Singh Negi et al 2025 New J. Phys. 27 103301

View the <u>article online</u> for updates and enhancements.

You may also like

- Structure and dynamics of a Rouse polymer in a fluctuating correlated medium Pietro Luigi Muzzeddu, Davide Venturelli and Andrea Gambassi
- Investigation of charge and ion drag force dynamics in complex plasma experiments with neon and argon under microgravity L Wimmer, S Beppler, N Dormagen et al.
- Avoiding barren plateaus via Gaussian mixture model
 Xiao Shi and Yun Shang

New Journal of Physics

The open access journal at the forefront of physics



Published in partnership with: Deutsche Physikalische Gesellschaft and the Institute of Physics



OPEN ACCESS

RECEIVED

23 May 2025

REVISED

13 October 2025

ACCEPTED FOR PUBLICATION

16 October 2025

PUBLISHED

29 October 2025

Original Content from this work may be used under the terms of the Creative Commons Attribution 4.0 licence.

Any further distribution of this work must maintain attribution to the author(s) and the title of the work, journal citation and DOI.



PAPER

Binary mixtures of intelligent active Brownian particles with visual perception

Rajendra Singh Negi^{1,2}, Roland G Winkler ond Gerhard Gompper to and Gerhard Gompper of the land of t

- ¹ Theoretical Physics of Living Matter, Institute for Advanced Simulation, Forschungszentrum Jülich, 52425 Jülich, Germany
- ² Department of Physics, Syracuse University, Syracuse, NY 13244, United States of America
- * Author to whom any correspondence should be addressed.

E-mail: g.gompper@fz-juelich.de

Keywords: binary mixture, self-steering particles, non-reciprocal interactions, visual perception, collective self-organization, active Brownian particles

Supplementary material for this article is available online

Abstract

The collective properties of a binary mixture of A- and B-type self-steering particles endowed with visual perception are studied by computer simulations. Active Brownian particles (ABPs) are employed with an additional steering mechanism, which enables them to adjust their propulsion direction relative to the instantaneous positions of neighboring particles, depending on the species, either steering toward or away from them. Steering can be nonreciprocal, in particular between the A- and B-type particles. The underlying dynamical and structural properties of the system are governed by the strength and polarity of the maneuverabilities (i.e. maximum reorientation torques) associated with the vision-induced steering. The model predicts the emergence of a large variety of nonequilibrium behaviors, which we systematically characterize for all nine principal sign combinations of AA, BB, AB and BA maneuverabilities. In particular, we observe the formation of multimers, encapsulated aggregates, honeycomb lattices, and predator-prey pursuit. Notably, for a predator-prey system, the maneuverability and vision angle employed by a predator significantly impacts the spatial distribution of the surrounding prey particles. For systems with electriccharge-like interactions (i.e. like-particles repel, unlike attract) and nonstoichiometric composition (i.e. small number excess of one component), we obtain at intermediate activity levels an enhanced diffusion compared to non-steering ABPs.

1. Introduction

Active-matter systems, ranging from microscopic biological systems such as bacteria [1–3] to macroscopic biological systems as flocks of birds [4–6], are intrinsically out of equilibrium and show a vast variety of fascinating emergent behaviors [7–10]. Such features are not restricted to biological systems, but have been partially reproduced in artificial and hybrid systems, specifically in those comprised of Janus colloids [11–13]. This makes active matter an important research field with significant biomedical potential, e.g. targeted drug delivery using engineered bacteria for tumor therapy [14] and biomedical untethered mobile milli/microrobots capable of accessing previously unreachable single cell sites for *in situ* and *in vivo* applications [15]. It also offers promising solutions for environmental improvements, such as water treatment [16, 17]. Arising patterns and structures not only depend on the physical interactions between the various agents of an ensemble, but are often governed by nonreciprocal sensing, e.g. directional visual perception in case of animals, processing of this information, and active self-steering response.

Multi-component mixtures of self-steering active agents with nonreciprocal interactions can show an even more intriguing behavior. It is important to note that the nonreciprocal nature of interactions in multi-component systems is on a different level compared to single-component systems, because the reaction of particles of one species to a particle of another species can be different from the inverse reaction [18–21].

Binary mixtures of active agents with nonreciprocal interactions are prevalent in biological systems. For example, mixed swarms of bacteria Bacillus subtilis and Pseudomonas aeruginosa exhibit both cooperation and segregation across scales [22]. Mixtures of two strains of B. subtilis with distinct cell aspectratios show aggregate formation, in which longer cells serve as nucleation sites, attracting shorter and highly mobile cells [23]. Mixing motile and nonmotile Escherichia coli bacteria results in activity-induced density modulations, where the circular movement of motile cells near surfaces creates flowing patterns that carry nonmotile cells along, while sedimentation disrupts vertical symmetry, crucial for their gathering [24]. Interactions between marine Pseudoalteromonas sp. and Gram-positive bacteria show predator-prey behavior, where the predator uses enzymes to kill Gram-positive cells while coexisting peacefully with Gram-negative bacteria, revealing how microbes can both compete and cooperate within mixed communities [25]. Recent experimental evidence indeed suggests that swimming and chemotactic sensing play an important role in shaping interbacterial interactions [26]. Furthermore, the relevance of sensing and self-steering is evident in macroscale binary biological systems. For instance, the flight of bee swarms to new nests consists of a binary mixture of streaker (leader) bees and follower (uninformed) bees, where bees use directed vision for attraction and repulsion among themselves [27, 28]. Also, there are many examples of large animals hunting others, like wolves chasing deer or sharks hunting fish swarms. In synthetic systems, chemotactic signaling in a mixture of microscale oil droplets of different chemistry embedded in micellar surfactant solutions have been shown to create predator-preylike nonreciprocal chasing interactions [21, 29, 30].

Theoretical and simulation studies of model systems provide essential insight into the complex emergent behavior of active systems in general and binary mixtures of self-steering particles in particular. They facilitate the characterization of the emergent structures and dynamics and their dependence on the agent properties. Ultimately, they can provide a guide for the rational design of synthetic active agents with desired properties.

Self-organization in active systems yields many emergent behaviors. 'Dumb' active Brownian particles (ABPs)—with conservative interactions only, like hard-core repulsion—display aggregation in the form of motility-induced phase separation (MIPS) [31–34] and nonequilibrium clustering [35]. The presence of (nonconservative) hydrodynamic interactions ('squirmers') [36] can induce additional behaviors, such as active turbulence [37, 38]. Already binary mixtures of active and passive Brownian particles show phase separation with domains enriched by passive or active particles, and propagating interfaces between them [39–42]. Experimental studies demonstrate that passive silica colloids rapidly self-assemble into tunable 2D structures via diffusiophoretic interactions with UV-activated Janus particles, with the clustering dynamics controlled by light intensity and particle size ratios [43]. Along the same line, simulations by varying the active particle density reveal a nonmonotonic clustering trend, where high activity leads to an effective screening of phoretic interactions, slowing down aggregation [44].

Systems of intelligent' self-steering particles display novel phenomena of dynamic self-organization. In systems with alignment of the propulsion direction of a particle with those of its neighbors, as in the Vicsek model [6], collective motion in single-component systems has been predicted in form of global polar order or travelling bands [6, 45]. The incorporation of anisotropic sensory perception in that model significantly impacts the system's collective behavior [46]. In single-component self-steering systems with pursuit-type steering, an even more complex behavior can emerge, such as milling [47, 48], and the formation of worm-like structures and worm-aggregate coexistence [47, 49–52]. Variants of the Vicsek model with two distinct species, for example systems of slow- and fast-moving self-propelled particles, where particles align within their own species and antialign with the other, yield micro-phase separation and parallel/antiparallel bands [53], while mixtures of active and passive particles with local alignment in confinement display segregation into an active core and a passive shell [54].

For mixtures of active particles with nonreciprocal interactions between particle types, the emergent behavior becomes even more intriguing. A prominent example is a mixture of chemically interacting particles, which produce or consume a chemical to which they are attracted or repelled corresponding to positive or negative chemotaxis. Such systems display a wealth of active clustering and phase-separation phenomena, such as association of particles into small molecules, aggregation into a static dense phase that coexists with a dilute phase, and the formation of nonstoichiometric self-propelled macroscopic clusters with a comet-like tail [55]. Self-propulsion heterogeneity and nonreciprocity of binary interactions can drive the partial segregation of mixtures of active colloids [56].

Here, we explore the collective behavior and structure formation of binary mixtures of active particles with visual perception and nonreciprocal self-steering. An agent is modeled as an 'intelligent' active Brownian particle (iABP), with implicit self-steering abilities. An iABP can move toward or away

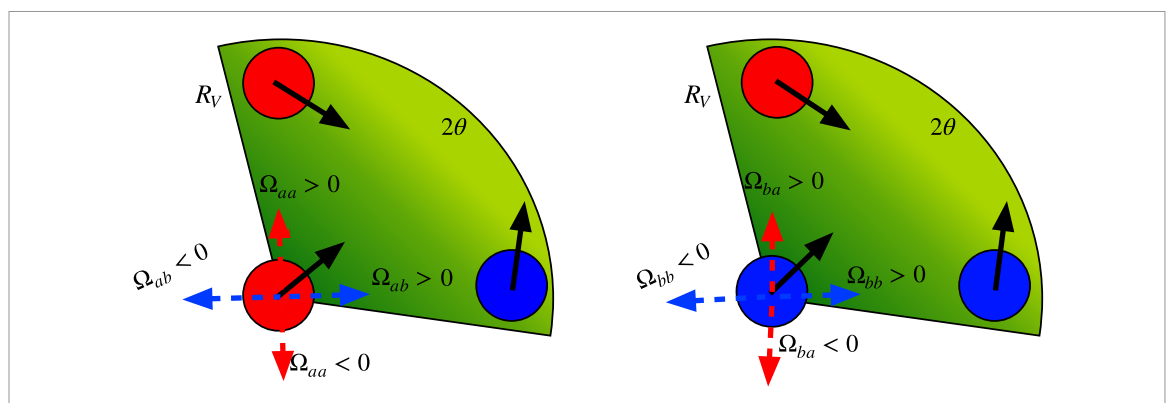


Figure 1. Schematic representation of the vision cone of a particle of the two types, A (red) and B (blue), and their corresponding maneuverabilities. The dashed arrows indicate the nature of steering toward and away from detected particles within the vision cone.

from its own or the other species, with limited maneuverability Ω , by sensing the positions of neighboring particles in its vision cone, as illustrated in figure 1. Our approach reaches well beyond previous studies, e.g. of chemically interacting droplets [55, 56], as the influence of directional sensing on the emergent structures and dynamics in binary systems is investigated, an aspect which plays a fundamental role in a wide range of biological systems. The considered generic model allows for a systematic variation of essential parameters, such as the vision angle and the maneuverabilities, and hence, the exploration of unique emergent features. Despite the applied minimal model, our approach contains a significant number of parameters, such as the activities of the two particle species, their vision angles and steering ability, the particle densities etc. This renders a comprehensive characterization challenging, so that we focus on various parameter combinations, which illustrate intriguing emergent behaviors. These combinations yield a rich phase behavior and interesting dynamics, such as multimeric aggregates, a predator-prey-type behavior, and the formation of a honeycomb-type lattice, structure, which are characterized and analyzed in detail.

2. Modeling binary mixtures of intelligent ABPs

2.1. Equations of motion

In our minimalistic approach, the two types A and B of agents are described as self-steering iABPs with visual perception. A mixture is composed of the total number $N = N_A + N_B$ of particles. The particle dynamics is governed by the equations of motion [47, 51, 57]

$$m\ddot{\mathbf{r}}_{i} = -\gamma_{\mathrm{T}}\dot{\mathbf{r}}_{i} + \mathbf{F}_{i}^{a}(t) + \mathbf{F}_{i} + \mathbf{\Gamma}_{i}(t), \qquad (1)$$

where $F_i^a(t) = \gamma_T v_0 e_i(t)$ is the propulsion force resulting in a speed v_0 along the direction $e_i(t)$, which can change in response to the sensed environment. Moreover, m is the mass of an iABP, γ_T the translational friction coefficient, and F_i the excluded-volume interactions between the iABPs. The latter are taken into account by the truncated and shifted Lennard–Jones potential

$$U_{IJ} = \begin{cases} 4\epsilon \left[\left(\frac{\sigma}{r} \right)^{12} - \left(\frac{\sigma}{r} \right)^{6} \right] + \epsilon, & r \leqslant 2^{1/6} \sigma \\ 0, & r > \sigma \end{cases}$$
 (2)

Here, σ is the particle diameter, ϵ the repulsion strength, and r the distance between two iABPs. Thermal fluctuations are considered as Gaussian and Markovian stochastic process Γ_i of zero mean and the second moments $\langle \Gamma_i(t) \cdot \Gamma_j(t') \rangle = 2d\gamma_T k_B T \delta(t-t') \delta_{ij}$ in d dimensions, with T the temperature and k_B the Boltzmann constant.

An iABP is capable to respond to information regarding the position of the neighboring particles within a vision cone by adjusting its propulsion direction. Figure 1 illustrates the vision cones for a *A*-(red) particle and a *B*- (blue) particle, respectively, along with their respective capability (maneuverability) to respond to the instantaneous positions of their neighbors.

The evolution of the propulsion direction $e_i^{\alpha}(t)$ of particle i of type α $(\alpha, \beta \in \{A, B\})$ is governed by [51, 58]

$$\dot{\boldsymbol{e}}_{i}^{\alpha}\left(t\right) = \sum_{\gamma \in \{\alpha,\beta\}} \boldsymbol{M}_{i}^{\alpha\gamma} + \boldsymbol{\Lambda}_{i}\left(t\right) \times \boldsymbol{e}_{i}^{\alpha}\left(t\right). \tag{3}$$

The last term describes the (thermal) rotational diffusion independent of the particle type. It is modeled as Gaussian and Markovian stochastic processes of zero mean, variance $\langle \mathbf{\Lambda}_i(t) \cdot \mathbf{\Lambda}_j(t') \rangle = 2(d-1)D_R\delta_{ij}\delta(t-t')$, and the rotational diffusion coefficient D_R .

The cognitive 'visual' torque $M_i^{\alpha\gamma}$ by particles of the same $(\gamma = \alpha)$ or different $(\gamma = \beta)$ type in the vision cone VC is [50, 51]

$$\boldsymbol{M}_{i}^{\alpha\gamma} = \frac{\Omega_{\alpha\gamma}}{N_{\alpha\gamma}} \sum_{i \in VC} e^{-r_{ij}^{\alpha\gamma}/R_{0}} \boldsymbol{e}_{i}^{\alpha} \times \left(\boldsymbol{u}_{ij}^{\alpha\gamma} \times \boldsymbol{e}_{i}^{\alpha}\right). \tag{4}$$

Here, $\mathbf{u}_{ij}^{\alpha\gamma} = \mathbf{r}_{ij}^{\alpha\gamma}/|\mathbf{r}_{ij}^{\alpha\gamma}|$ is the unit vector of the distance $\mathbf{r}_{i}^{\alpha} - \mathbf{r}_{j}^{\gamma}$ between particle i and j of the types α and γ , and

$$N_{\alpha\gamma} = \sum_{j \in VC} e^{-r_{ij}^{\alpha\gamma}/R_0} \tag{5}$$

is the normalization factor, which is determined by the effective number of such particles in the vision cone. The condition for particles i to lie within the vision cone of particle i is

$$\mathbf{u}_{ii}^{\alpha\gamma} \cdot \mathbf{e}_{i}^{\alpha} \geqslant \cos\theta_{\alpha},\tag{6}$$

where θ_{α} —the vision angle—is the opening angle of the vision cone centered by the particle orientation e_i^{α} , and R_0 describes the characteristic range of the visual perception. Additionally, the vision range is limited to

$$|\mathbf{r}_i^{\alpha} - \mathbf{r}_i^{\gamma}| \leqslant R_{\nu},\tag{7}$$

treating all particles further apart than R_v as invisible $(R_v \geqslant R_0)$. In a dilute system, only a single particle may be within the distance R_v , and the exponential factor $\mathrm{e}^{-r_{ij}^{\alpha\gamma}/R_0}$ cancels out, as it appears both in the numerator and denominator in equation (4). Conversely, in a dense system, an effective reduced vision range R_0 appears due to the exponential factor. This can be interpreted as blocking the view by neighboring particles highlighting the influence of the local environment on visual perception (similar to the effect studied in [5]).

The torque $M_i^{\alpha\gamma}$ describes the preference of an iABP to move toward [47, 51] or away [59, 60] from the center of mass of iABPs of type γ in its vision cone VC, depending on the sign of the maneuverability $\Omega_{\alpha\gamma}$. The normalization equation (5) implies a nonadditive interaction, and emphasizes the importance of the effective particle number in the vision cone. It is motivated by the fact that additive and nonadditive interactions imply distinct macroscopic behaviors in interacting active systems [61].

We want to emphasize that our model contains four mechanisms of nonreciprocal behavior: (i) Directed sensing in the vision cone (in particular for small vision angles, where one agent might see another, but not vice versa); (ii) the nonadditivity of the interaction (as two interacting particles may have different effective numbers of neighbors); (iii) the nonreciprocity in the steering torques given by equations (3) and (4), which are nonsymmetrical under an exchange of particles i and j already at the two-particle level, even for panoramic view (vision angle $\theta = \pi$); and, of course (iv) the different reaction of A-agents to B-agents compared of B- to A-agents (reflected in the different maneuverabilities $\Omega_{AB} \neq \Omega_{BA}$).

We focus here on two-dimensional systems. Then, with the representation of the propulsion direction in polar coordinates, $\boldsymbol{e}_{i}^{\alpha}=(\cos\varphi_{i}^{\alpha},\sin\varphi_{i}^{\alpha})^{\mathrm{T}}$ and the difference vector $\boldsymbol{u}_{ij}^{\alpha\beta}=(\cos\varphi_{ij}^{\alpha\beta},\sin\varphi_{ij}^{\alpha\beta})^{\mathrm{T}}$, equation (3) implies the equation of motion for the orientation angle φ_{i}^{α}

$$\dot{\varphi}_{i}^{\alpha} = \sum_{\gamma \in \{\alpha, \beta\}} \frac{\Omega_{\alpha\gamma}}{N_{\alpha\gamma}} \sum_{j \in VC} e^{-r_{ij}^{\alpha\gamma}/R_{0}} \sin\left(\phi_{ij}^{\alpha\gamma} - \varphi_{i}^{\alpha}\right) + \Lambda_{i}(t), \tag{8}$$

with Λ_i a Gaussian and Markovian stochastic process of zero mean and $\langle \Lambda_i(t) \Lambda_j(t') \rangle = 2D_R \delta_{ij} \delta(t-t')$. Although we consider a minimal model, the system contains a significant number of parameters, as there is the Péclet number $Pe = \nu_0/(\sigma D_R)$ (where σ is the effective particle diameter) the vision angles θ_α ($\alpha \in \{A,B\}$), the vision range R_0 and cut-off radius R_v , the maneuverabilities $\Omega_{\alpha\beta}$, the packing fraction $\Phi = \pi \, \sigma^2 N/(4L^2)$ (with linear systems size L), and the particle numbers N_α , with $\alpha \in \{A,B\}$. This gives rise to a rich phase behavior and interesting dynamics.

2.2. Parameters

We measure lengths in units of the particle diameter σ , time in units of $\tau = \sqrt{m\sigma^2/(k_BT)}$, and energies in units of the thermal energy k_BT [47, 51].

The friction coefficient γ_T is chosen as $\gamma_T = 10^2 \sqrt{mk_BT/\sigma^2}$, the rotational diffusion coefficient as $D_R = 8 \times 10^{-2} \sqrt{k_BT/(m\sigma^2)}$, which yields the relation $D_T/(\sigma^2D_R) = 1/8$ with $D_T = k_BT/\gamma_T$. These choices ensure that inertia effects are negligible, since the small ratio $mD_R/\gamma_T = 8 \times 10^{-4} \ll 1$ implies a strongly overdamped single-particle dynamics [63]. The activity of the iABPs is characterized by the Péclet number

$$Pe = \frac{v_0}{\sigma D_{\rm R}}. (9)$$

The adaptation of the interaction strength $\epsilon/k_BT=(1+Pe)$ warrants a nearly constant iABP overlap during iABP contacts, even at high activities [47]. Periodic boundary conditions are applied. The equations of motion (1) are integrated with a velocity-Verlet-based scheme suitable for stochastic systems [64], using the time step $\Delta t=10^{-3}\tau$. The maneuverabilities $\Omega_{\alpha\beta}$ are scaled with D_R , such that $\Omega_{aa}=\Omega_{AA}/D_R$ etc. If not stated otherwise $R_0=1.5\sigma$ and $R_v=4R_0$. We consider two types of initial conditions for the system: in the first case, both A and B particles are randomly distributed throughout the simulation box; in the second case, the particles are arranged on a square lattice in an alternating ABAB pattern in the center of the simulation box, with iABP distances equal to their diameter in the center of the simulation box, with iABPs distances equal to their diameter σ . In both cases, the initial propulsion directions of all particles are randomly assigned.

We performed 10⁷ relaxation steps, and collect data for the subsequent 10⁷ steps. For certain averages, up to 10 independent realizations are considered.

2.3. Phases and phase diagrams

Figure 2 presents an overview of emerging phases for nine combination of the maneuverabilities $\Omega_{\alpha\beta}$, with equal magnitude and all possible sign combinations. In each case, the three Péclet numbers Pe = 1.25, 5.0, 12.5 and three vision angles $\theta_A = \theta_B = \theta = \pi, \pi/4, \pi/8$ are investigated. Various kinds of complex structures are obtained, such as mixed aggregates, segregated aggregates, layers of aggregates of one type of iABPs surrounded by a homogeneous layer of the other type of iABPs, homogeneous aggregates engulfed by the another type of iABPs, dimers, mixed states, and honeycomb lattice-type structures.

In the following sections, the emerging structures and their dynamics will be discussed for several parameter combinations in more detail.

3. Avoiding same, favoring opposite type of intelligent ABPs

3.1. Structures

A system, in which particles of the same type steer away and of opposite type steer toward each other, i.e. $\Omega_{aa} = \Omega_{bb} < 0$ and $\Omega_{ab} = \Omega_{ba} > 0$, bears some similarity with an electrostatic system, where equally charged particles repel and different charged particles attract. This analogy implies that the formation of 'charge' dipoles (dimers) can be expected. Snapshots of the typical conformations are displayed for $\Omega_{aa} = \Omega_{bb} = -\Omega_0$ and $\Omega_{ab} = \Omega_{ba} = +\Omega_0$ with $\Omega_0 = 12.5$ in Figure 2(g), and for $\Omega_0 = 62.5$ in figure 3. The emergent structures strongly depend on the vision angle and the Péclet number, as illustrated in Figure 3(a) for equal particle numbers $N_A = N_B$. For the small maneuverability $\Omega_0 = 12.5$ and low Pe, figure 2(g), as well as for $\Omega_0 = 62.5$ and all Pe, figure 3, hetero-dimers form for the large vision angle $\theta=\pi$, as for electrostatic interactions. Nevertheless, no dimer pairs, chains, or clusters are found, as might be expected from the electrostatic analogy. This is a consequence of the polarity of the iABPs by their propulsion direction, which breaks the spatial isotropy of their mutual interactions, although vision itself is isotropic and stabilizes dimers, but leads to a repulsive interaction between them, so that the average distance between dimers is determined by the particle densities $\rho_A = N_A/L^2 = N_B/L^2 = \rho_B$ of iABPs. For a homogeneous spatial distribution of particles, the average distance d_p between dimers can be estimated from the density as $d_{\rm p}=(4/\pi)^{1/2}\rho_A^{-1/2}\approx 5\sigma$ (for N=1000 and L=100 as well as N = 625 and L = 78.5), in good agreement with simulation results. In contrast, for the small vision angle $\theta = \pi/16$, an iABP detects only other iABPs in a narrow vision cone and disordered structures of single particles are observed, especially for small Pe, as found in non-steering systems.

For vision angles $\pi/8$ and $\pi/4$, larger Péclet numbers, and the higher maneuverability $|\Omega_{\alpha\alpha}| = |\Omega_{\alpha\beta}| = 62.5$, self-organized patterns appear, see figure 3(a). Even hexagonally close-packed structures

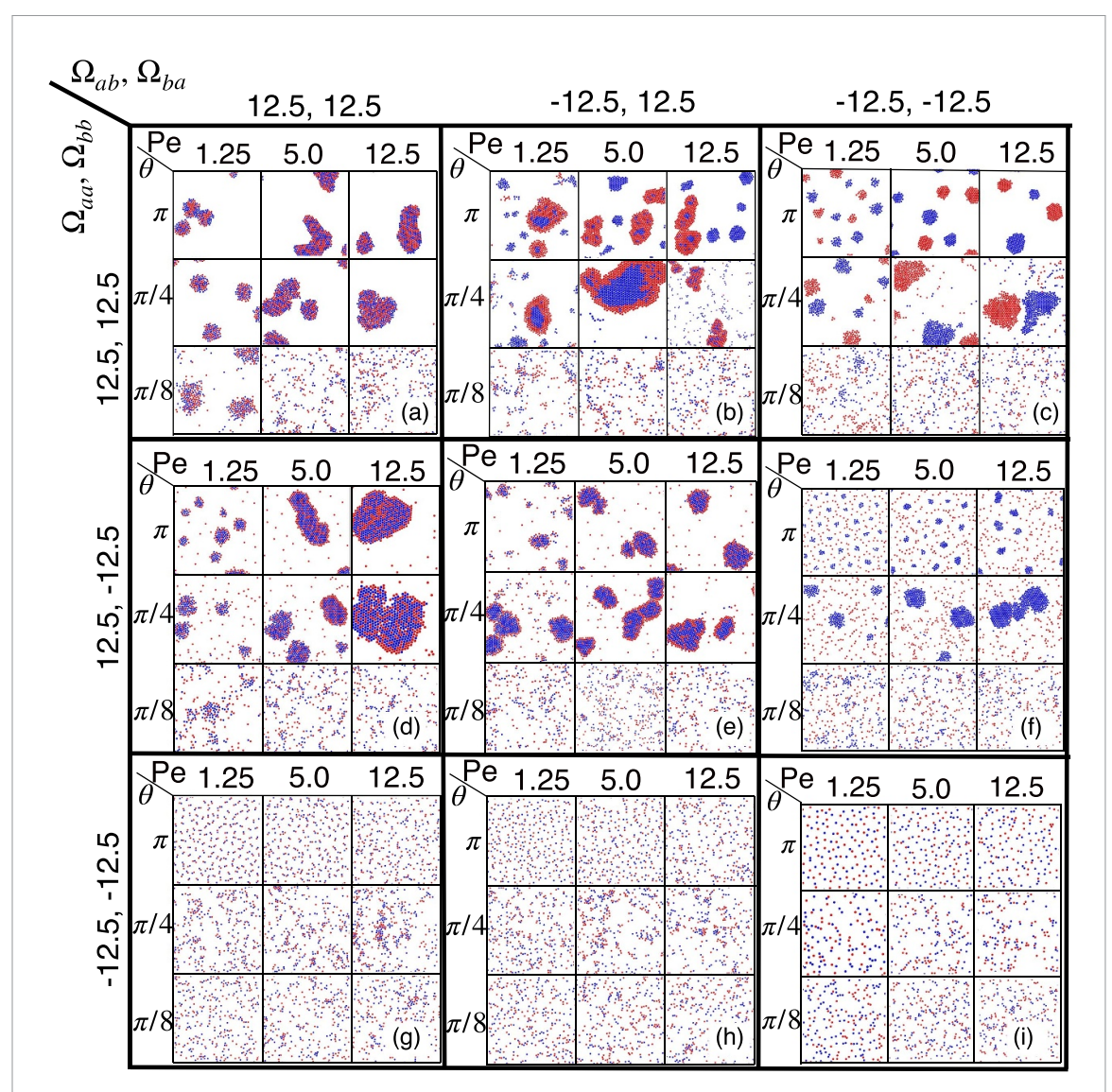


Figure 2. Snapshots of phases for 9 combinations of the maneuverabilities and the Péclet numbers 1.25, 5.0, and 12.5, and vision angles π , $\pi/4$, and $\pi/8$. The number of particles is $N_A = N_B = N/2 = 500$ at the packing fraction $\Phi = 0.0785$. (see also movie M1 [62].)

are formed for large *Pe*. Specifically, double layers of similar iABPs reflect the nonreciprocal character of the interactions.

It is of course also interesting to consider nonstoichiometric systems, where one particle type, say A, is the minority component, i.e. $N_A < N_B$. Figure 3(b) illustrates the influence of the number ratio N_A/N_B at constant overall packing fraction on structure formation. Instead of A–B pairs, now clusters with a larger number of B-type iABPs appear. With increasing majority component B, clusters grow and several layers of B-type iABPs may form around A particles. The cluster size is limited by (i) the number of minority iABPs, and (ii) the vision range. For $\theta = \pi/4$ and $\pi/8$ and not too large ratios $N_B/N_A \approx 3$ and 7, similar layered structures of A- and B-type particles appear as for the stoichiometric case (at the same Pe = 12.5), although with a smaller number on A-type iABPs. For large vision angles $\theta \geqslant \pi/2$, the formation of triplets, septuplets, and larger aggregates is observed.

The (average) polarity field, determined by the orientation of the propulsion direction, in any cluster points preferentially toward a center of a cluster, although with some deviations in case of the opposite multilayers, see figure 3(a). In particular, the clusters in figure 3(b) for $N_A/N_B = 5/620$ and $\theta = \pi$ with a single central A-particle are very stable (see movie M3). The B-type particles all point toward the central A particle, because the effective torque on a B particle by its neighboring B particles is close to zero, as (i) the torque on head-to-tail arranged particles with parallel propulsion direction is zero (see equation (4)), and (ii) the torque of the side-by-side arranged iABPs also nearly vanished due to their hexagonal arrangement. That leaves a residual preferred motion toward the A particle. Furthermore, the

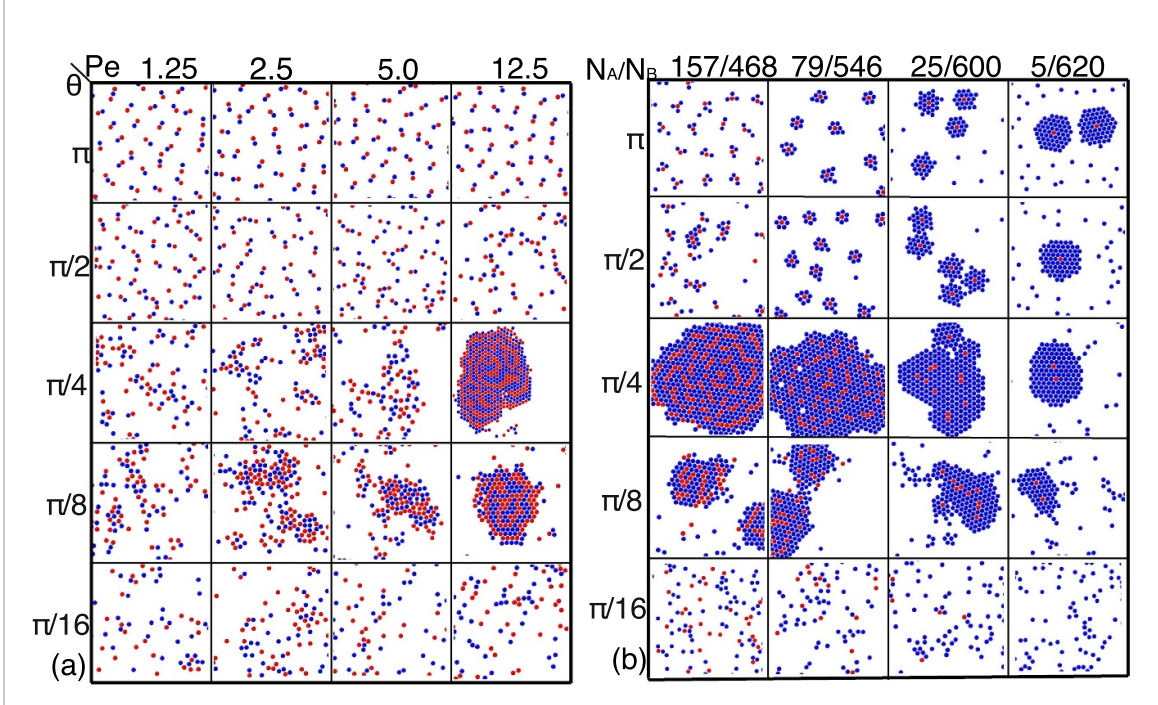


Figure 3. Snapshot of phases for the maneuverabilites $\Omega_{aa} = \Omega_{bb} = -62.5$ and $\Omega_{ab} = \Omega_{ba} = 62.5$ and various combinations of (a) vision angle $\theta_A = \theta_B = \theta$ and Péclet number Pe for $N_B = N_A = 312$, and (b) and the ratio of the number N_A/N_B of the two types of iABPs and the vision angle for the Péclet number Pe = 12.5. The packing fraction is $\Phi = 0.0785$. (see also movie M2 and M3 [62].)

dispersed B particles in the gas phase surrounding a cluster repel those inside the cluster and thereby stabilize the phase separation. The vision range, which is $R_V = 4R_0 = 6\sigma$ in figure 3(b), plays an important role for this cluster formation and cluster size, as B-particles within the vision range are attracted to the A-particle in the cluster center.

3.2. Dynamics

To characterize the dynamical features of iABP self-organization, we consider their mean-square displacements (MSD)

$$\langle \mathbf{r}^{2}(t)\rangle = \frac{1}{N} \sum_{i=1}^{N} \left\langle (\mathbf{r}_{i}(t+t_{0}) - \mathbf{r}_{i}(t_{0}))^{2} \right\rangle, \tag{10}$$

where the average is performed over the initial time t_0 . For vision angles $\theta \leqslant \pi/2$, the dynamics shows an ABP-like behavior, with a ballistic motion for times $D_R t < 10$ and a diffusive motion for longer times, see figure 4(a). To characterize the dynamics as a function of vision angle and Péclet number, we extract an effective translational diffusion coefficient D_L from the long-time MSD, as displayed in figure 4(b) as a function of the vision angle. Here, the maneuverabilities are $\Omega_{aa} = \Omega_{bb} = -\Omega_0$ and $\Omega_{ab} = \Omega_{ba} = +\Omega_0$, with $\Omega_0 = 62.5$; these values are used throughout this section unless stated otherwise.

For large vision angle $\theta = \pi$, the MSD is very small due to the formation of dimeric clusters. The self-propulsion of dimers is 'suppressed', because the propulsion directions point preferentially toward each other, as in a MIPS of ABPs. In contrast to the latter, steering prevents a diffusive change of the propulsion direction and the pairs are stable for a long time.

The narrower vision cone for $\theta=\pi/2$ can cause intermittent loss of mutual perception between particles in a dimer due to rotational noise. This disruption weakens the stabilizing steering torques, thereby reducing the overall stability of the dimers. Consequently, dimers at $\theta=\pi/2$ are less stable and the formed structures are more disordered, also larger temporary string-like (polymer-like) aggregates appear. The corresponding MSD is larger than that for $\theta=\pi$, but smaller than that for a non-steering ABP due to the formation of small clusters. Interestingly, an enhanced diffusion is also observed for the vision angles $\theta=\pi/4$ and $\pi/8$, which can be attributed to temporarily formed small clusters with highly inhomogeneous particle orientations, where the restricted rotational diffusion due to vision interaction causes a slightly enhanced persistent motion. Finally, at the very small vision angle $\theta=\pi/16$, where

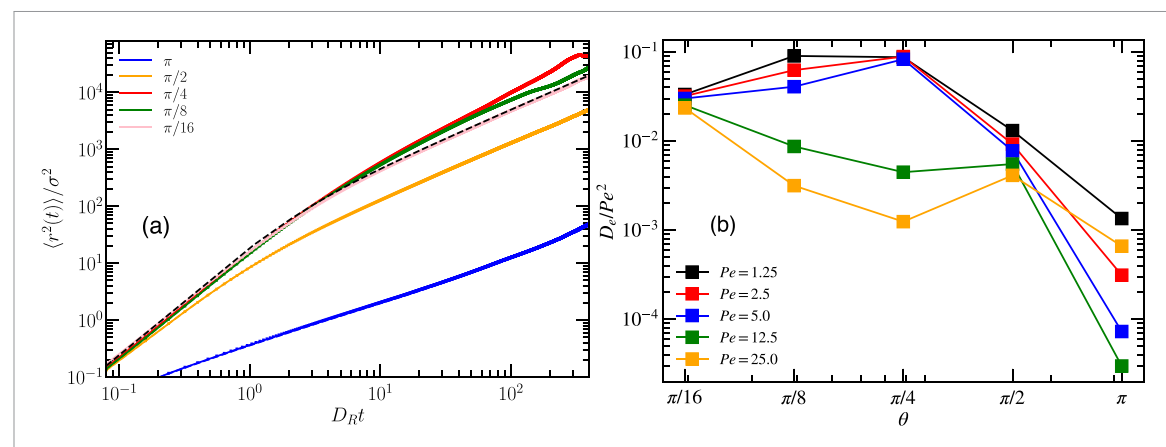


Figure 4. Dynamics of iABPs. (a) Mean squared displacement (MSD) as a function of scaled time $D_R t$ for Pe = 5.0 and various vision angles θ . The black dashed line represents the MSD of non-steering ABPs. (b) Effective diffusion coefficient $D_e = D_L/D_R$ extracted from the MSD, scaled by the square of the Péclet number, as a function of the vision angle θ for various Pe. The number ratio is $N_B/N_A = 312/313$, the packing fraction is 0.0785, and the maneuverabilities are $\Omega_{aa} = \Omega_{bb} = -\Omega_0$ and $\Omega_{ab} = \Omega_{ba} = +\Omega_0$, with $\Omega_0 = 62.5$.

an iABP detects hardly any other iABPs, the system is in a disordered dilute phase, where the particles exhibit the same MSD as individual non-steering ABPs.

This behavior is of course also reflected in the results for the diffusion coefficient $D_{\rm e}=D_{\rm L}/D_{\rm R}$, see figure 4. It first increases with increasing θ , then decreases for $\theta\gtrsim\pi/4$, as long as $Pe\lesssim5.0$. In his range of Pe values, $D_{\rm e}$ is nearly independent of Pe, because motion is dominated by the translational diffusion of dimers. For larger Péclet numbers, Pe=12.5 and 25.0, large aggregates are present for $\theta=\pi/4$ and $\pi/8$ (compare figure 3(a)), where the total propulsion is reduced by partial compensation of the particle activity. The N_e 'passivated' particles in the cluster diffuse with an effective diffusion coefficient $\sim 1/N_e$, which reduces the overall diffusion coefficient. Interestingly, $D_{\rm e}$ is larger for $Pe\leqslant5.0$ and $\theta\leqslant\pi/2$ than for larger Pe, in particular for Pe=25.0. This happens, because higher Pe stabilizes propulsion directions toward the cluster center. Finally, for $\theta=\pi/16$, the diffusion coefficients are well fitted by the relation $D_{\rm e}=D_{\rm L}/D_{\rm R}\sim Pe^2=v_0^2/(\sigma^2D_{\rm R}^2)$ of non-steering ABPs.

The clusters in figure 3(a) for $\theta = \pi/4$ and Pe = 12.5, and those in figure 3(b) for $\theta = \pi$ and $N_A/N_B = 620/5$ exhibit an interesting collective dynamics. In the first case, a pronounced rotational motion appears due to a polarization of the propulsion directions. In the second case, the near-hexagonal arrangement of the *B*-type particles leads to a compensation of propulsion forces, and the cluster translates only very slowly with very little rotation.

3.3. Hopping

In the nearly stoichiometric case, with $N_B = N_A + N_{\rm d}$ and $N_{\rm d} \ll N_A$, A-B dimers dominate in the conformations but are accompanied by $N_{\rm d}$ unpaired iABPs. These unpaired particles can shuttle between dimers and exchange places with particles within the dimers. Hence, we denote such an unpaired particle as a hopper and the corresponding dynamical regime is hereafter referred to as the 'hopping phase'. The transport of unpaired particles resembles the Grotthuss mechanism of proton transport from one water molecule to another via the formation and breaking of hydrogen bonds [65]. However, the transport of hoppers between dimers is by active motion and not by hydrogen bond rearrangements along a network, as in the Grotthuss mechanism [65]. Here, the maneuverabilities are $\Omega_{aa} = \Omega_{bb} = -\Omega_0$ and $\Omega_{ab} = \Omega_{ba} = +\Omega_0$, with $\Omega_0 = 62.5$; these values are used throughout this section unless stated otherwise.

Figure 5 shows sequences of such hopping events, where a particle from a pair is replaced by a hopper, resulting in the formation of a new pair. To define a hopper, we use a distance criterion—as long as a particle is not within the distance $h_d = 1.5\sigma$ of another particle, it is a hopper. The dynamics of hoppers depends on the Péclet number, the packing fraction, and the number $N_d = |N_B - N_A|$ of excess B-or A-type particles beyond stoichiometry.

3.3.1. Hopper number, encounter distance, displacement, and hopping time

Figures 6(a) and (b) show the average number N_{hopp} of hoppers present in the system at various activities and packing fractions. Interestingly, at small Pe = 1.25 the number of hoppers is larger compared to higher Pe, and increases only slightly as the number difference N_{d} increases. This larger number N_{hopp} is

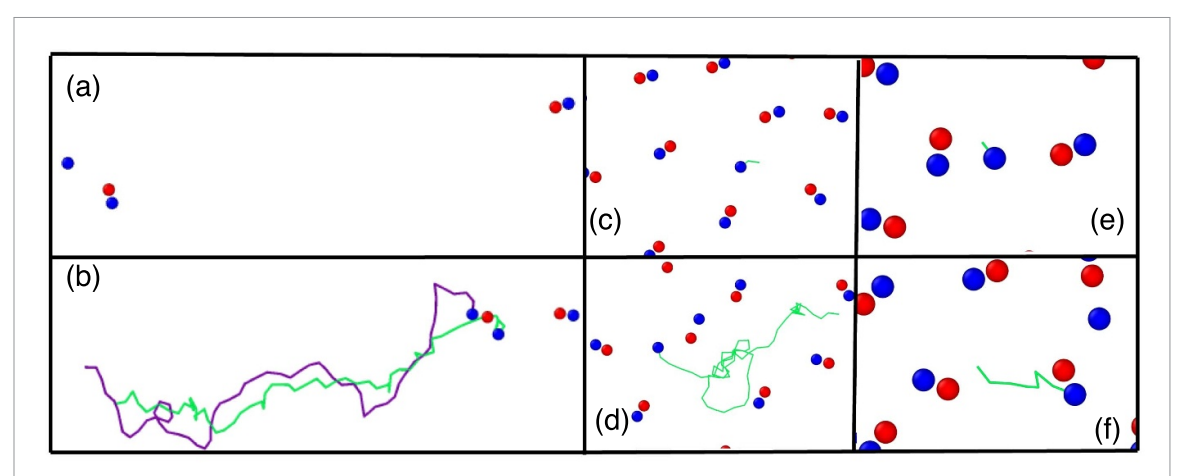


Figure 5. Snapshots of the hopper-pair exchange dynamics. The depicted sequences illustrate the replacement of a particle within a pair by a 'hopper', leading to the formation of a new hopper. In each sequence, only the trajectories of the hopper and the two particles in the pair it interacts with are highlighted for clarity. (a), (c), (e) Initially, a blue hopper, steers toward the red particle of a pair at the packing fractions (a), (b) $\Phi = 0.007\,85$, (c), (d) $\Phi = 0.039\,25$, and (e), (f) $\Phi = 0.0785$. (b), (d), (f) Subsequently to an exchange, a blue hopper traverse the green trajectory and substitutes another blue particle within the pair. The parameters used are $N_d = 5$, Pe = 12.5, $\Omega_{aa} = \Omega_{bb} = -\Omega_0$, and $\Omega_{ab} = \Omega_{ba} = +\Omega_0$, with $\Omega_0 = 62.5$ (see movie M4 [62].)

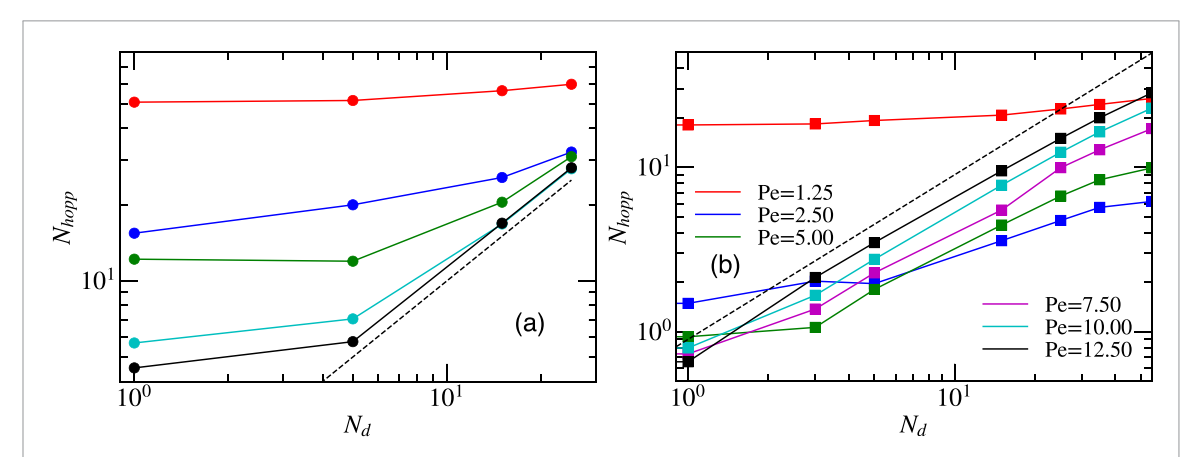


Figure 6. Activity dependence of the number of hoppers. Number N_{hopp} of hoppers as a function of the number difference $N_{\text{d}} = N_B - N_A$ for various Péclet numbers (Pe) and the packing fractions (a) $\Phi = 0.00785$ and (b) $\Phi = 0.0785$. The dashed lines correspond to $N_{\text{hopp}} = N_{\text{d}}$. The maneuverabilities are $\Omega_{aa} = \Omega_{bb} = -\Omega_0$ and $\Omega_{ab} = \Omega_{ba} = +\Omega_0$, with $\Omega_0 = 62.5$.

due to thermal noise. Despite opposite-type particles steering toward each other, noise disrupts their sustained proximity, and suppresses long-time stable pair formation, which results in the creation of many hoppers. At the low density $\Phi=0.00785$ (figure 6(a)), the number of hoppers decreases with increasing activity, as dimers become more stable. N_{hopp} decreases with increasing packing fraction at fixed Pe and N_{d} , as the distance between dimers decreases and they become less susceptible to a particle exchange (see figures 6(a) and (b)). For the higher packing fraction $\Phi=0.0785$ (figure 6(b)), N_{hopp} is smaller than for the lower packing fraction (figure 6(a)) (at a given Pe and N_{d}). Due to the larger density, hoppers are more likely to meet dimers, but the exchange process takes longer, which results in more stable clusters of three particles and, hence, a reduced number of hoppers. At large Pe and N_{d} —the latter number depends on the packing fraction— N_{hopp} increases approximately linearly with the number difference, which suggest that approximately all minority-type A particles are bound in pairs.

To further characterize the hopping behavior in the process of the formation of a new pair, we calculate the average hopping time Δt and the average hopping displacement $|\Delta r|$. The results of these quantities, presented in figure 7, reflect a distinct density dependence. For higher packing fractions, hoppers traverse small distances only and thus have a high encounter probability with A–B pairs or other free particles, which expedites the hopper-transfer process. Conversely, for lower packing fraction, the hopping times increase similar to the increasing increased distances. The shortest average hopping time occurs at Péclet number Pe = 1.25, again due to the importance of noise. As particles in a pair are loosely attached to each other, hoppers can easily break a pair and generate a new pair and a new hopper. As the activity increases ($Pe \lesssim 5.0$), dimers are more stable and the hopping time increases. For even

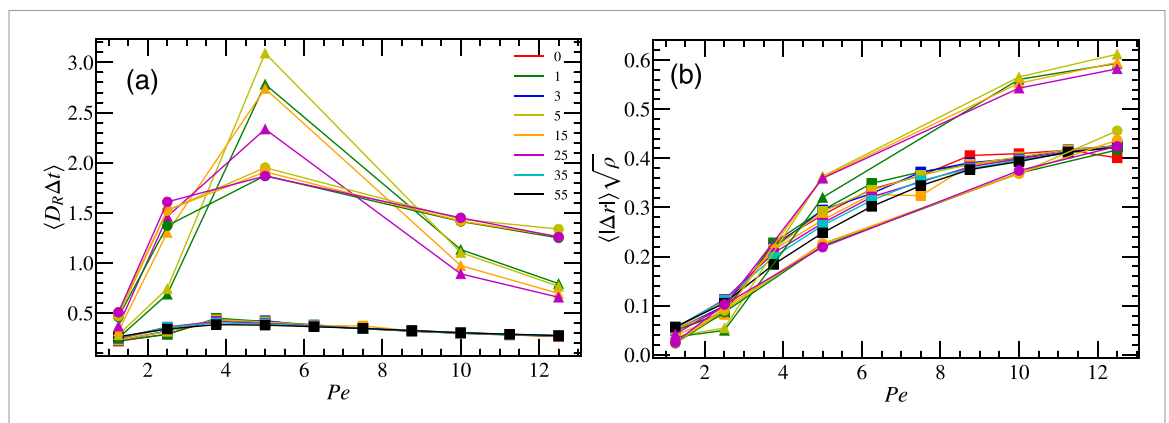


Figure 7. Characteristic average life times and displacements of hoppers as a function of Péclet number and for various number differences $N_{\rm d}$ (legend). (a) Average hopping time $\langle D_{\rm R} \Delta t \rangle$, during which a hopper is unbound before combining with other particles, and (b) average scaled displacement $\langle |\Delta r| \rangle \sqrt{\rho}$ as a function of the Péclet number Pe for various number difference $N_{\rm d}$ (see legend). Here, $\rho = (N_A + N_B)/L^2$ is the number density of iABPs. Packing fractions are indicated by different symbols, with $\Phi = 0.0785$ (squares), 0.03925 (triangles), and 0.00785 (bullets). The maneuverabilities are $\Omega_{aa} = \Omega_{bb} = -\Omega_0$ and $\Omega_{ab} = \Omega_{ba} = +\Omega_0$, with $\Omega_0 = 62.5$.

larger Pe, $D_R \Delta t$ is almost constant or decreases with in increasing Pe, depending on density, due to the enhanced persistent motion of the iABPs.

The simulation results for the hopping time Δt suggest that it is mainly determined by the distance a hopper covers before exchanging with another pair, see figure 7(a). This is different for the displacement $|\Delta r|$ displayed in figure 7(b), which scales very well with the average dimer distance $1/\sqrt{\rho}$, and increases monotonically with increasing Péclet number and saturates for large Pe. Notably, $|\Delta r|$ is very similar for the largest and smallest considered packing fraction. Moreover, the two quantities presented in figures 7(a) and (b) are independent of the number difference for packing fraction $\Phi = 0.0785$ and $\Phi = 0.00785$.

Remarkably, the systems at the intermediate packing fraction $\Phi=0.03925$ exhibit a different behavior. First, the average hopping time depends on the number difference. Second, the maximum average hopping time is larger than the values for the larger and smaller packing fractions. We conjecture that this is an effect of finite dimer density and their spatial distribution. At the intermediate particle density, hoppers are typically nearly equidistant from surrounding dimers, hence the selection of and motion toward the closest dimer is accidental, which leads to intermittent caging and longer paths. In addition, pairs are more responsive to an approaching hopper compared to higher density systems. Thus, a hopper requires a longer time to reach a dimer and replace a paired iABP.

3.3.2. MSD: caging and chasing

To characterize the dynamics of iABPs in the 'hopping phase', we evaluate the MSD of the A and B particles. The characterization of the dynamics of hoppers itself is only possible for rather short times due to frequent recombination and exchange with A–B pairs. The presence of the majority B component affects the dynamics of the mixture. Depending on the parameters, we find short- and intermediate-time regimes with sub- and super-diffusive behavior—the long-time dynamics (with $D_R t \gtrsim 40$) is always diffusive. The various MSD regimes are differentiated by their power-law time dependent MSD $t^{\alpha_{1,2}}$, with exponents α_1 in the short-time ($D_R t < 2$) and α_2 in the intermediate-time ($2 < D_R t < 20$) regime.

Figures 8(a) and (b) show values of the exponent $\alpha_{1,A}$ of A (minority) and $\alpha_{1,B}$ of B (majority) particles for the large packing fraction $\Phi=0.0785$. The values $\alpha_{1,A}<1$ (see figure 8(a)) reflect a subdiffusive nature of the minority A particles, which are typically paired with B particles, which repel other B particles and thus exhibit a caging effect (see figures 2(g) and 3(b)). The exponent $\alpha_{1,A}$ decreases with increasing activity as the propulsion directions in these dimeric pairs are more strongly aligned toward each other, which reduces the overall (active) dynamics. The weak dependency on $N_{\rm d}$, with the lowest value of $\alpha_{1,A}$ at large $N_{\rm d}=55$ and the highest at low $N_{\rm d}=1$, can be attributed to the fact that the larger the number difference the smaller is the long-time stability and mobility of individual dimers.

The majority *B*-type iABPs exhibit nearly diffusive behavior for $N_d \lesssim 5$ and Pe < 2.5 (see figure 8(b)). However, the exponent $\alpha_{1,B}$ decreases with increasing Pe. This is a consequence of the more stable A-B pairs at larger Pe, which leads to a drop in the number of (highly mobile) hoppers (see figure 6). The A and B particles exhibit then a similar, cage-determined diffusive behavior (cf figure 8(b)). With

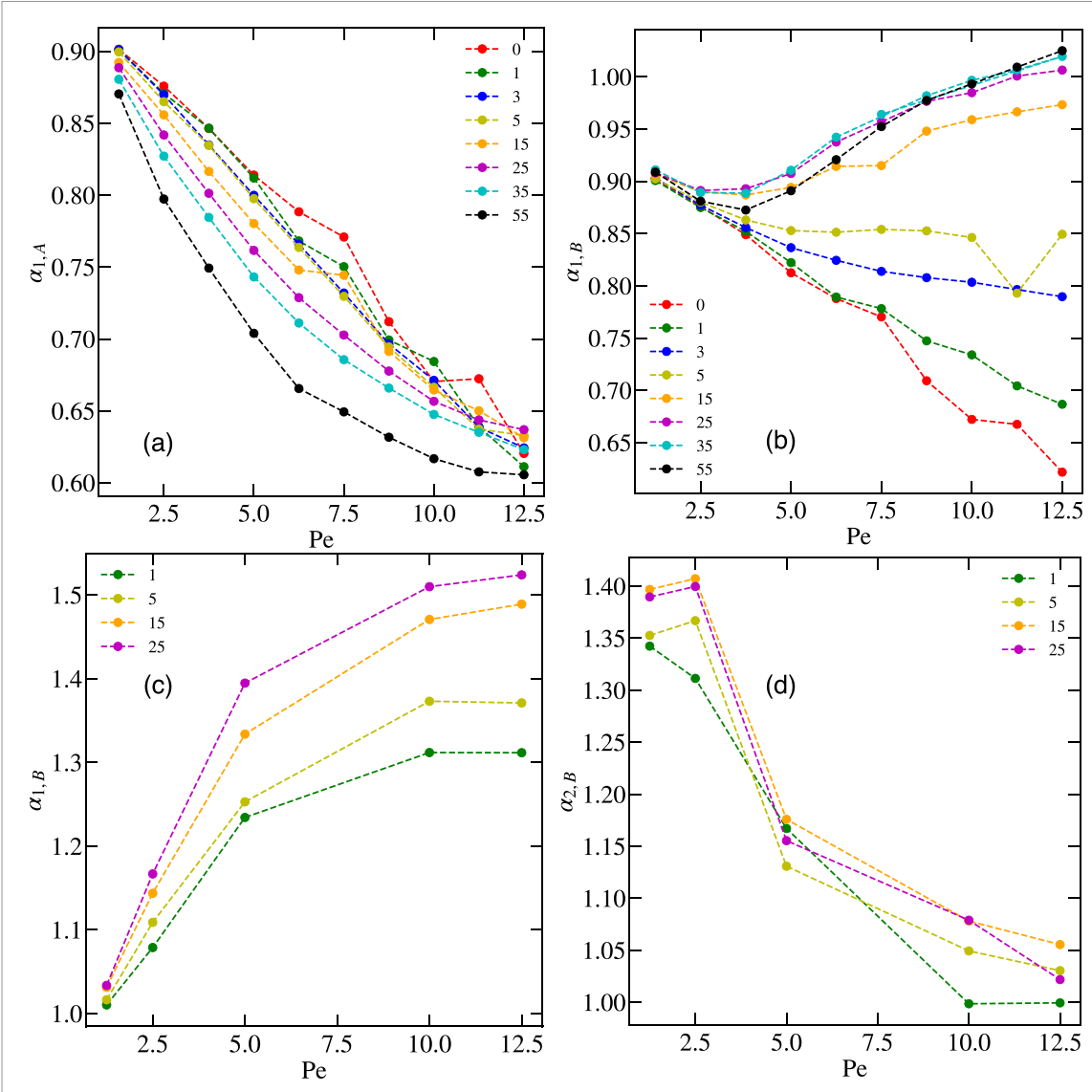


Figure 8. Dynamics of A- and B-type iABPs, characterized by the MSD exponent $MSD \sim t^{\alpha}$ for the short and intermediate time range. (a) Exponents $\alpha_{1,A}$ for A (minority) particles and (b) $\alpha_{1,B}$ for B (majority) particles at the packing fraction $\Phi=0.0785$; (c) exponents $\alpha_{1,B}$ and (d) $\alpha_{2,B}$ for B particles at the packing fraction $\Phi=0.00785$ as a function of the Péclet number Pe and various $N_{\rm d}$ (legend). The total number of particles is $N=N_A+N_B=625$ and the maneuverabilities are $\Omega_{aa}=\Omega_{bb}=-\Omega_0$ and $\Omega_{ab}=\Omega_{ba}=+\Omega_0$, with $\Omega_0=62.5$.

increasing N_d , more free hoppers are present (figure 6) and $\alpha_{1,B}$ increases, approaching the diffusion limit $\alpha_{1,B} = 1$ for $N_d \gtrsim 15$, nearly independent of the Péclet number.

The dynamics of the iABPs is rather different in the dilute systems with packing fraction $\Phi=0.00785$. The minority A particles are as mobile as the B particles, consequently the values of the exponents are $\alpha_{1,B}\approx\alpha_{1,A}$ and $\alpha_{2,B}\approx\alpha_{2,A}$. In fact, the MSD is smaller for Bs than for As, because the opposing propulsion directions in pairs reduce the activity contribution to their dynamics. Propulsion implies a super-diffusive dynamics at short and intermediate time scales, with exponents $\alpha_{1,B}>1$ (for Pe>2.5) and $\alpha_{2,B}>1$ (for Pe<10.0), where an increasing activity leads to an increasing exponent at short times (see figure B(c)) and a decreasing exponent for intermediate times (see figure B(d)). The growth of the exponent B(a) and a decreasing exponent for intermediate times (see figure B(d)). The growth of the exponent B(d) and a decreasing exponent for intermediate times (see figure B(d)). The growth of the exponent B(d) are an enhanced mobility of the iABPs by the increasing activity, in analogy to that of ABPs. Interestingly, hoppers can chase A-B pairs (compare figure B), in which the propulsion directions turn approximately in the same direction, hence, leads to an enhanced dynamics of the hopper and the pair. As B(d) increases, the number of hoppers which chase a pair increases, thus, the effective mobility of both increases too, which is reflected in a growth of the exponent B(d). In the intermediate time regime, B(e) hoppers are super-diffusive at small Péclet numbers. This is explained by an activity-enhanced dynamics as in the short-time regime for large B(e). With increasing B(e), the activity-enhanced time regime shifts to shorter times, and in the intermediate regime

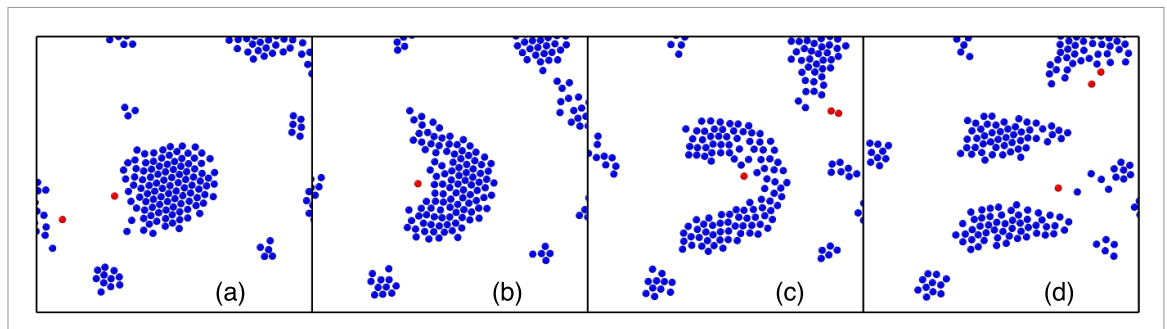


Figure 9. Snapshots of a predator-prey pursuit. Series of snapshots (zoomed) progressing in time from (a)–(d), which illustrate a typical pursuit of a predator (red) chasing prey particles (blue). The parameters are $N_B/N_A = 50/1$, $\theta_A = \pi/4$, $\theta_B = \pi$, $\Omega_{aa} = \Omega_{bb} = 12.5$, $\Omega_{ab} = 12.5$, $\Omega_{ba} = -12.5$, and the number of particles $N_A + N_B = 1000$. (see also movie M5 [62]).

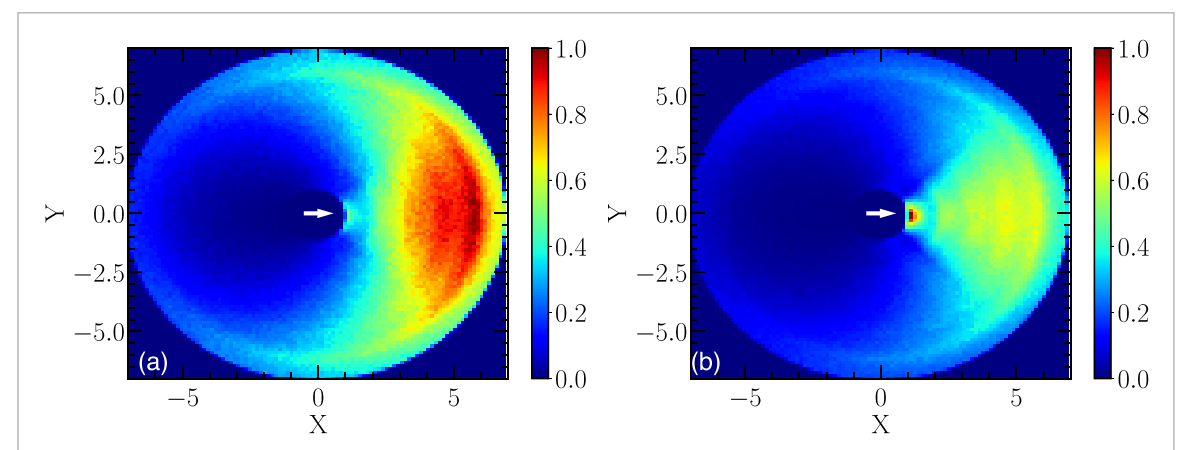


Figure 10. Distribution of prey particles around a predator (*A*) for the predator maneuverabilities (a) $\Omega_{ab} = 12.5$ and (b) $\Omega_{ab} = 50$. The white arrow in the center indicates the predator's moving direction. The other parameters are $\Omega_{aa} = \Omega_{bb} = 12.5$, $\Omega_{ba} = -12.5$, Pe = 1.25, P

hoppers exhibit the long-time diffusive behavior, which is only weakly dependent on the number difference $N_{\rm d}$.

4. Predator-prey behavior

When like-particles attract each other, while A particles chase B particles, which try to escape from A particles—with maneuverabilities $\Omega_{aa}=\Omega_{bb}=+\Omega_0$, and $\Omega_{ab}=-\Omega_{ba}=\Omega_0$ —a predator-prey-type of collective behavior is observed. This combination of the signs of maneuverabilites leads to the formation of cohesive groups and clusters by the same kind of particles (compare figure 2(b)). We consider here a system, where the vision angles of the two particle types are *not* the same, but a vision angle of the predator (θ_A) which is smaller than that of the prey $(\theta_B=\pi)$. Note that throughout this simulation study we always consider the case where the Péclet numbers of A and B particles are the same, so that also here the speeds of predator and prey are the same. The emerging clusters can be considered as 'hunting packs' of type-A particles chasing 'herds' of prey-like type-B particles. Figure 9 displays a sequence of snapshots illustrating a typical pursuit scenario (see also movie M5). Clearly, the prey particles form various coexisting clusters, while the number of predator particles is too small for the formation of larger clusters. As time moves on, the predator approaches a prey cluster, and the prey particles try to escape, while the predator maintains its moving direction until the prey cluster has dispersed and the predator encounters another prey cluster.

The spatial distribution of prey particles around a predator is displayed figure 10 for various maneuverabilities $|\Omega_{ab}|$, averaged over several encounters of predator and prey. The distribution of prey is symmetric in the direction perpendicular to the predator's moving direction and asymmetric along the propulsion direction, with a depletion of the number of prey particles behind the predator. As the prey senses the predator, it steers away from it. Since the small vision angle of the predator, here $\theta_A = \pi/4$, provides only a limited view on the prey and its steering maneuverability, $|\Omega_{ab}| = 12.5$, is low, the predator moves toward the prey in front, and most other prey can escape sidewise and keep at a reasonable

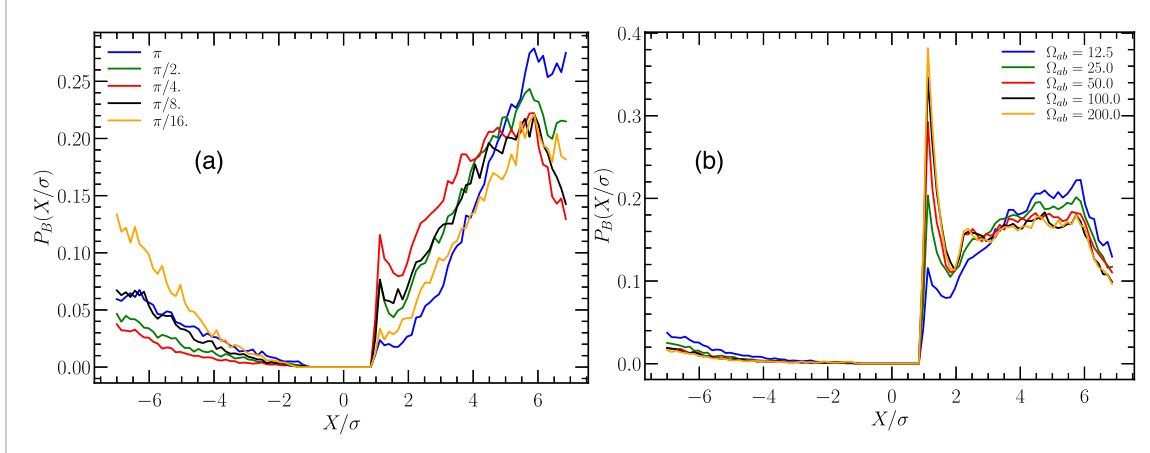


Figure 11. Normalized prey distribution $P_B(X/\sigma)$ in the direction of motion of the predator (*A*) for (*a*) various vision angles θ_A and $\Omega_{ab} = 12.5$, and (b) various maneuverabilities and $\theta_A = \pi/4$. The other parameters are the same as in figure 9.

distance of approximately 4.5σ from the predator. However, when the predator's steering maneuverability is increased to $|\Omega_{ab}| = 50$, the predator can catch up with the prey more easily, and move closer to the prey.

A quantitative characterization of the prey distribution in the moving direction of the predator is shown in figure 11 for various vision angles θ_A (figure 11(a)) and maneuverabilities $|\Omega_{ab}|$ (figure 11(b)). The prey distribution $P_B(X/\sigma)$ is defined as the mean number of prey particles (B) observed along the direction of motion (X) of a predator (A), averaged over time and contributing particles. As a predator moves closer to a group of prey, prey particles sensing the predator disperse first by moving sidewise and reconvene later. Due to the cohesion of the prey cluster, even prey particles outside of the vision range of the predator move away from it and become depleted in its vicinity. As expected, there is a substantial accumulation of prey in front of the predator $(X \ge 0)$, whereas the number of prey particles is reduced behind the predator ($X \le 0$). Here, the vision angle θ_A of the predator plays an important role (figure 11(a)). For small predator vision angles, such as $\theta_A = \pi/16$, the visual field is narrow, which implies a reduced prey detection and subsequently low prey densities in front of the predator. As θ_A increases to $\pi/8$ and $\pi/4$, the prey density in front reaches its maximum. A further increase to $\theta_A \geqslant \pi/2$ leads again to a decline of the prey density, because the predator now senses prey everywhere and therefore cannot easily decide on the most promising direction of motion. Hence, the optimal vision angle of a predator to hunt prey lies around $\pi/4$, which provides focused vision ('eagle's eye'). The broader field of view for $\theta_A \geqslant \pi/2$ counteracts an effective chasing of the prey, because the simultaneous visibility of prey in many different directions implies a less goal-oriented and more erratic motion of the predator.

The dependence of predation efficiency on the predator maneuverability Ω_{ab} is displayed in figure 11(b), illustrated the prey distribution, P_B for predator vision angle $\theta_A = \pi/4$. Again, an asymmetric distribution evolves, which is characterized by an accumulation of prey in front of the predator and scarcity behind, as expected. At large predator maneuverability, $|\Omega_{ab}| = 200$, the probability for the predator to approach prey particles closely is very high, because the predator can rapidly adjust its direction of motion, optimizing its chance of catching the prey. This probability diminishes significantly as the maneuverability decreases to $|\Omega_{ab}| \lesssim 25$, because the predator struggles to efficiently position itself in relation to the prey and to mimic its escape motions, resulting in a reduced probability to come close to the prey.

We have not studied finite-size effects systematically. Systems with 50 and 1000 (prey) particles (with the same number density) display very similar behaviors, which indicates that finite-size effects are small.

5. Honeycomb-lattice-type structure formation

We want to illustrate the enormous variability of self-organization in mixtures of self-steering active agents with nonreciprocal interactions by briefly discussing another intriguing phase, a quasi-periodic, honeycomb-lattice-like structure. Such a phase is obtained when one particle type (B) wants to aggregate, the other (A) to disperse, while different types want to avoid each other. This happens for the maneuverabilities $\Omega_{aa} = -\Omega_{bb} < 0$, and $\Omega_{ab} = \Omega_{ba} < 0$. Figure 12 displays snapshots for $N_A = N_B$, which reflect the dependence of the emerging lattice on the vision cut-off range R_v (see also figure 2(f)). When the vision cut-off range is small (figure 12(a), $R_v = 4.0\sigma$), particle segregation is weak, only small

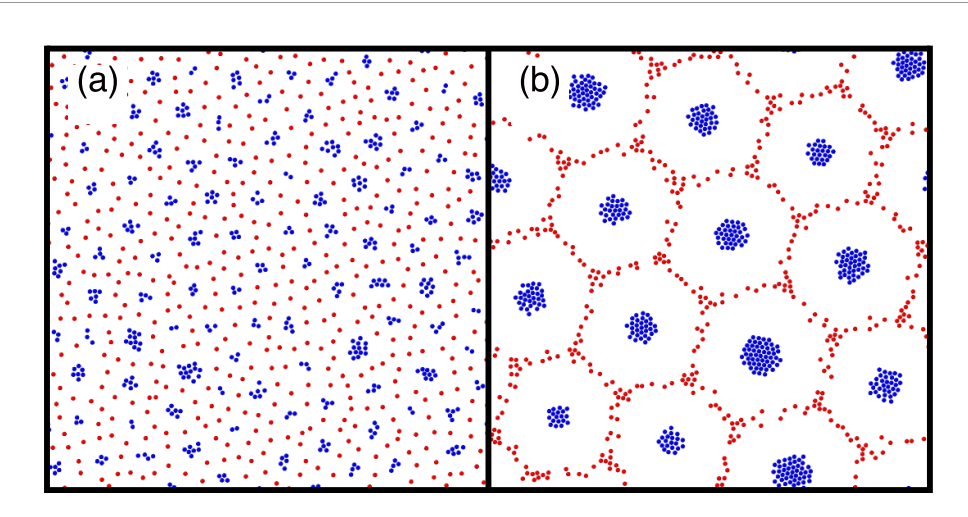


Figure 12. Snapshots of honeycomb-type lattices. The various structures follow by varying the vision range R_v , where in (a) $R_v = 4.0\sigma$, and (b) $R_v = 14.0\sigma$. The maneuverabilities are $\Omega_{aa} = -12.5$, $\Omega_{aa} = 12.5$, $\Omega_{ab} = \Omega_{ba} = -12.5$. Furthermore, Pe = 1.25, $N_A + N_B = 1000$, $\theta_A = \theta_B = \pi$, and $\Phi = 0.0785$. (see also movie M6 [62]).

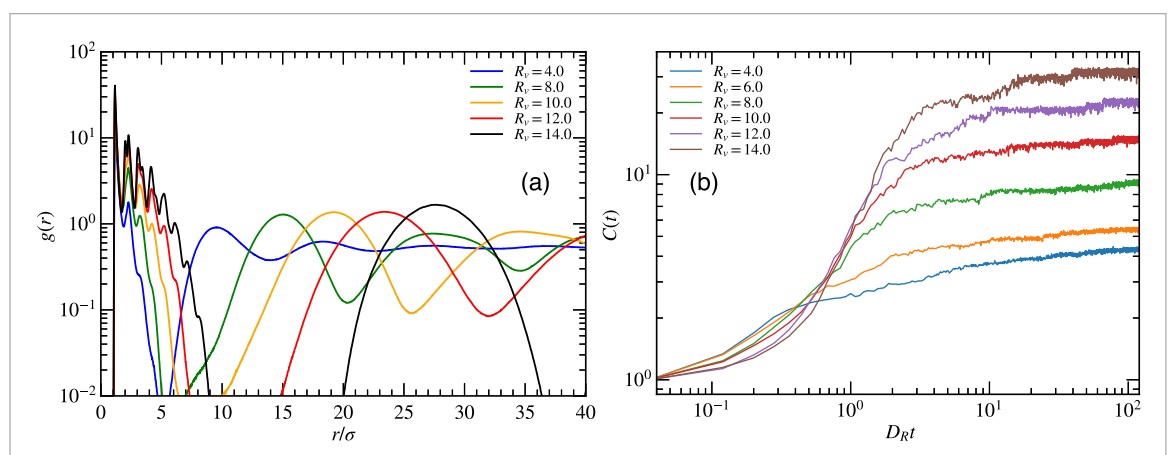


Figure 13. (a) Pair correlation-function g(r) of B particles as a function of the radial distance for various vision cut-off radii R_v (legend). (b) Average number C(t) of B iABPs in a cluster as a function of the scaled time $D_R \Delta t$ for various vision cut-off radii R_v . The Péclet number is Pe = 1.25. The other parameters are the same as in figure 12.

clusters from and locally diffuse honeycomb-like structures appear. As the vision range increases to $R_{\nu}=14.0\sigma$ (figure 12(b)), a pronounced and well-defined honeycomb lattice is formed. This extension of the cut-off range increases the number of particles in specific areas, the lattice structure becomes better defined, and a noticeable number of particles cluster together in the center of each hexagon as well as along its edges. Thus, the visual interaction range can play a crucial role in the formation of particular structures of iABPs.

Figure 13(a) displays the pair correlation-function for B particles, which demonstrates the prevalence of the honeycomb lattice structures. At small R_v , small cluster of B particles are formed and a fluid-like distribution appears at distances $r/\sigma > 5$. With increasing R_v , the core clusters grows with pronounced peaks at the various B particle layers. In addition, a broad peak grows and shifts to larger distances with increasing R_v , indicating the position of the first hexagonal shell of neighboring B particle clusters, where its width accounts for the average number of B particles in the respective clusters.

It is also interesting to consider the dynamics of the structure formation of the honeycomb lattices. Starting from a uniform distribution of iABPs, we determine the average size of B clusters and their growth for the various cut-off radii R_v . A particle is considered part of a cluster if the distance with another particle in the cluster is $r \le 1.5\sigma$. Figure 13(b) illustrates the average cluster growth. At short times $D_R t < 0.1$, all systems exhibit a similar behavior independent of R_v . However, for longer times $D_R t > 1$, clusters are formed, which grow with time until they reach a stationary state. For the cut-off range $R_v = 4\sigma$, the average cluster contains about four particles and there are many clusters (figure 12(a)). The clusters are very dynamic and reform continuously. The cluster size gradually

increases with increasing vision cut-off range, reaching approximately 30 iAPBs for $R_{\rm v}=14\sigma$. It is important to note that the coarsening effectively stops because the A particles in the hexagon boundaries present an efficient barrier for the crossing of B particles. Thus, the hexagonal structure is very stable despite its dynamic nature.

The honeycomb lattice-like structures appear at lower activity levels (Pe = 1.25), while at higher activities Pe = 5.0, 12.5, as seen in figure 2(f), the lattice breaks down, giving way to more cohesive, clustered structures predominantly composed of one particle type. As Pe increases, the particles exhibit a faster and more persistent motion, which likely disrupts the delicate interplay of interactions necessary to sustain the quasi-crystalline honeycomb arrangement.

6. Summary and conclusions

We have studied binary mixtures of self-steering active particles with nonreciprocal interactions, where particle motion and steering is based on the instantaneous position of neighboring particles, using a minimal cognitive model. The particle speed, vision angle, vision range, and sign and strength of maneuverability—relative to their peers and the foreign species—all play crucial roles in the self-organization and structure formation. Beyond a general overview of the enormous variability of emerging structures, we focus on the dynamical properties of three interesting self-organized phases, multimeric aggregates in off-stoichiometric mixtures, prey-predator-type behavior, and the formation of honeycomb-type lattices.

In steering systems, where unlike types attract and like types repel (section 3), the number ratio of the two components plays a crucial role in the structure formation, along with the vision angle and the propulsion speed. These interactions leads to the formation of molecular structures, such as dimers and tetramers at low density—reminiscent to structures in systems with electric charges and reciprocal interactions—, and to higher multimeric aggregates for higher densities. However, the dynamics of the systems with reciprocal and nonreciprocal interactions is very different. For numbers of ABPs, which deviate slightly from stoichiometric ratios, unpaired particle display a hopping dynamics between multimers, where they can knock out a particle in the existing aggregate and substitute it, resulting in a sub-diffusive (caged) behavior at short times and diffusing motion at a longer time. The analysis of the mean hopping displacement shows a strong density dependence, where a high/low-density system has the smallest/highest hopping displacement.

In the case of a nonreciprocal steering response between the two particle types, i.e. $\Omega_{ab} = -\Omega_{ba}$, and only one of the types (the 'prey') preferring the vicinity of their peers, the emergent dynamics displays a predator-prey-like behavior. Our analysis reveals that the optimal angle for the predator to steer toward the prey is around $\pi/4$, corresponding to focused vision, which allows the predator to steer effectively toward the prey without getting distracted to much by other prey. Our simulation results are strikingly similar to the behavior of some natural systems, like reef shark in a fish swarm [66]; this type of predator-prey behavior has actually already been employed [67] to construct congestion avoidance for multiple micro-robots. Our results should provide the necessary guidance to optimize the design of such micro-robotic systems.

Finally, we considered a similar case with nonreciprocal *A*–*B* interactions as before, but now its only the predators which look for the vicinity of their peers. This seemingly small change generated a completely different kind of self-organization, where predator clusters to form a very stable honeycomb lattice with the vision cut-off range determining the size of the cluster and the lattice constant—with larger clusters for larger vision range.

Our system displays some fundamental and phenomenological similarities with mixtures of chemically interacting particles, which produce or consume a chemical to which they are attracted or repelled [55]. In both cases, nonequilibrium nonreciprocal interactions between particles, which break action-reaction symmetry lead to new classes of active phase separation phenomena. For example, the formation of molecule-like binary aggregates, and of honeycomb-like lattices are observed in both systems. However, a closer look reveals also several important differences. First, interactions in the chemical system are isotropic, while our iABPs have directed sensing through the vision cone with a limited vision angle. Secondly, motion in the chemical systems develops as a results of chemotactic motion, while ABPs move with constant speed; the latter implies that iAPBs can only react to gathered information by steering, for which we impose a limited maneuverability. These differences imply strikingly different emergent structure formation and dynamics. For example, hopping 'defects' in the phase of small molecule-like aggregates in only seen for iABPs, as well as the animal-like predator-prey behavior. In contrast, static cluster of one particle type propelled by corona and tail of the other particle type are only seen in the chemical system.

A comparison of our results with biological systems is of course highly desirable, but not straightforward, because it requires a detailed characterization of the biological agents in terms of Péclet numbers, maneuverabities, directional sensing, etc. A important advantage of our 'minimalist' model of binary cognitive particle mixtures is its flexibility, which facilitates the description of a large variety of natural [68] and artificial [67, 69] systems. Here, (micro)robotic systems are very promising experimental model systems, as they allow the implementation of many different, simple or complex, interaction and steering rules. For example, a recent study [69] of a binary systems of programmable robots with nonreciprocal interactions, where species *A* aligns with *B* but *B* anti-aligns with *A* demonstrates the emergence of a collective chiral motion that can be stabilized by limiting the robot angular speed to be below a threshold. Moreover, colloidal model systems of externally controlled self-propelled particles [70] could be adapted easily to binary systems.

It will also be interesting to explore and utilize possible synergies between agent-based models and Cahn–Hillard-type continuum field theoretical approaches [71–73] to elucidate the behavior of nonreciprocal multi-component systems. For systems with directional sensing, such as visual perception, these approaches should include local polarization fields to capture the anisotropic nature of the interactions.

It is worth mentioning that the model can also be extended to systems in which particles are able to also change their type through reaction or interconversion, as discussed in [74, 75] for several species of droplets with varying sizes.

The extension of single-component cognitive active particle systems to nonequilibrium two-component mixtures with nonreciprocal interactions generates an enormous richness of emergent complexity and variability of self-organization and dynamical scenarios. Despite of several recent studies, the large space of self-organization behavior has just been scratched at the surface so far, and more detailed studies to elucidate the underlying physical mechanisms are required.

Data availability statement

The data that support the findings of this paper are openly available at the following URL/DOI: https://doi.org/10.5281/zenodo.15208145. [76].

Movie captions available at https://doi.org/10.1088/1367-2630/ae140c/data1.

ORCID iDs

Rajendra Singh Negi © 0000-0002-6522-166X Roland G Winkler © 0000-0002-7513-0796 Gerhard Gompper © 0000-0002-8904-0986

References

```
[1] Berg H C 1975 Nature 254 389-92
 [2] Be'er A, Ilkanaiv B, Gross R, Kearns D B, Heidenreich S, Bär M and Ariel G 2020 Commun. Phys. 3 66
 [3] Aranson I S 2022 Rep. Prog. Phys. 85 076601
 [4] Cavagna A and Giardina I 2014 Annu. Rev. Condens. Matter Phys. 5 183-207
 [5] Pearce D J, Miller A M, Rowlands G and Turner M S 2014 Proc. Natl Acad. Sci. USA 111 10422-6
 [6] Vicsek T, Czirók A, Ben-Jacob E, Cohen I and Shochet O 1995 Phys. Rev. Lett. 75 1226
 [7] Elgeti J, Winkler R G and Gompper G 2015 Rep. Prog. Phys. 78 056601
 [8] Bechinger C, Di Leonardo R, Löwen H, Reichhardt C, Volpe G and Volpe G 2016 Rev. Mod. Phys. 88 045006
[9] Gompper G et al 2020 J. Phys.: Condens. Matter 32 193001
[10] Gompper G et al 2025 J. Phys.: Condens. Matter 37 143501
[11] Park B W, Zhuang J, Yasa O and Sitti M 2017 ACS Nano 11 8910-23
[12] Bäuerle T, Fischer A, Speck T and Bechinger C 2018 Nat. Commun. 9 1-8
[13] Bastos-Arrieta J, Revilla-Guarinos A, Uspal W E and Simmchen J 2018 Front. Robot. AI 5 97
[14] Yan S, Zeng X, Wang Y and Liu B F 2020 Adv. Healthcare Mater. 9 2000046
[15] Sitti M, Ceylan H, Hu W, Giltinan J, Turan M, Yim S and Diller E 2015 Proc. IEEE 103 205-24
[16] Fu Y, Yu H, Zhang X, Malgaretti P, Kishore V and Wang W 2022 Micromachines 13 295
[17] Hu J, Zhou S, Sun Y, Fang X and Wu L 2012 Chem. Soc. Rev. 41 4356-78
[18] You Z, Baskaran A and Marchetti M C 2020 Proc. Natl Acad. Sci. 117 19767-72
[19] Saha S, Agudo-Canalejo J and Golestanian R 2020 Phys. Rev. X 10 041009
[20] Osat S and Golestanian R 2023 Nat. Nanotechnol. 18 79-85
[21] Meredith C H, Moerman P G, Groenewold J, Chiu Y J, Kegel W K, van Blaaderen A and Zarzar L D 2020 Nat. Chem. 12 1136–42
[22] Natan G, Worlitzer V M, Ariel G and Be'er A 2022 Sci. Rep. 12 16500
[23] Wang Q, Frye J G, McClelland M and Harshey R M 2004 Mol. Microbiol. 52 169-87
[24] Burriel S E and Colin R 2023 bioRxiv 2023-05
[25] Tang B L et al 2018 Nat. Commun. 11 285
[26] Seymour J R, Brumley D R, Stocker R and Raina J B 2024 Trends Microbiol. 32 640-9
```

- [27] Fetecau R and Guo A 2012 Bull. Math. Biol. 74 2600-21
- [28] Beekman M, Fathke R L and Seeley T D 2006 Anim. Behav. 71 161-71
- [29] Sengupta A, Kruppa T and Löwen H 2011 Phys. Rev. E 83 031914
- [30] Cira N J, Benusiglio A and Prakash M 2015 Nature 519 446-50
- [31] Bialké J, Speck T and Löwen H 2012 Phys. Rev. Lett. 108 168301
- [32] Wysocki A, Winkler R G and Gompper G 2014 Europhys. Lett. 105 48004
- [33] Cates M E and Tailleur J 2015 Annu. Rev. Condens. Matter Phys. 6 219-44
- [34] Digregorio P, Levis D, Suma A, Cugliandolo L F, Gonnella G and Pagonabarraga I 2018 Phys. Rev. Lett. 121 098003
- [35] Peruani F, Deutsch A and Bär M 2006 Phys. Rev. E 74 030904
- [36] Theers M, Westphal E, Qi K, Winkler R G and Gompper G 2018 Soft Matter. 14 8590-603
- [37] Qi K, Westphal E, Gompper G and Winkler R G 2022 Commun. Phys. 5 49
- [38] Goh S, Westphal E, Winkler R G and Gompper G 2025 Phys. Rev. Res. 7 013142
- [39] Stenhammar J, Wittkowski R, Marenduzzo D and Cates M E 2015 Phys. Rev. Lett. 114 018301
- [40] Wysocki A, Winkler R G and Gompper G 2016 New J. Phys. 18 123030 [1-9]
- [41] Wittkowski R, Stenhammar J and Cates M E 2017 New J. Phys. 19 105003
- [42] Kolb T and Klotsa D 2020 Soft Matter 16 1967-78
- [43] Singh D P, Choudhury U, Fischer P and Mark A G 2017 Adv. Mater. 29 1701328
- [44] Jhajhria M, Sahoo S, Biswas T and Thakur S 2023 Soft Mater. 21 1-14
- [45] Chaté H, Ginelli F, Grégoire G and Raynaud F 2008 Phys. Rev. E 77 046113
- [46] Gao Z and Couzin I D 2025 Phys. Rev. Res. 7 023144
- [47] Negi R S, Winkler R G and Gompper G 2024 Phys. Rev. Res. 6 013118
- [48] Saavedra R, Gompper G and Ripoll M 2024 Phys. Rev. Lett. 132 268301
- [49] Couzin I D, Krause J, James R, Ruxton G D and Franks N R 2002 J. Theor. Biol. 218 1-11
- [50] Barberis L and Peruani F 2016 Phys. Rev. Lett. 117 248001
- [51] Negi R S, Winkler R G and Gompper G 2022 Soft Matter. 18 6167-78
- [52] Liu Z and Dijkstra M 2025 Soft Matter. 21 1529-44
- [53] Chatterjee S, Mangeat M, Woo C U, Rieger H and Noh J D 2023 Phys. Rev. E 107 024607
- [54] Agrawal N K and Mahapatra P S 2021 Phys. Rev. E 104 044610
- [55] Agudo-Canalejo J and Golestanian R 2019 Phys. Rev. Lett. 123 018101
- [56] Maity S and Morin A 2023 Phys. Rev. Lett. 131 178304
- [57] Das S, Gompper G and Winkler R G 2018 New J. Phys. 20 015001
- [58] Goh S, Winkler R G and Gompper G 2022 New J. Phys. 24 093039
- [59] Negi R S, Iyer P and Gompper G 2024 Sci. Rep. 14 9443
- [60] Iyer P, Negi R S, Schadschneider A and Gompper G 2024 Commun. Phys. 7 379
- [61] Chepizhko O, Saintillan D and Peruani F 2021 Soft Matter. 17 3113-20
- [62] See supplemental material for simulation movies
- [63] Mandal S, Liebchen B and Löwen H 2019 Phys. Rev. Lett. 123 228001
- [64] Grønbech-Jensen N and Farago O 2013 Mol. Phys. 111 983-91
- [65] Agmon N 1995 Chem. Phys. Lett. 244 456-62
- [66] A picture of a reef shark in a school of fish was taken in 2012 in Australia by Scott Carr (available at: https://iso.500px.com/parting-of-the-feast-behind-this-remarkable-photo-of-a-reef-shark-parting-a-school-of-fish/)
- [67] Touahmi Y, Burlutskiy N, Lee K and Lee B 2012 Int. J. Adv. Robot. Syst. 9 67
- [68] Tsang A C, Demir E, Ding Y and Pak O S 2020 Adv. Intell. Syst. 2 1900137
- [69] Chen J, Lei X, Xiang Y, Duan M, Peng X and Zhang H P 2024 Phys. Rev. Lett. 132 118301
- [70] Lavergne F A, Wendehenne H, Bäuerle T and Bechinger C 2019 Science 364 70-74
- [71] Fruchart M, Hanai R, Littlewood P B and Vitelli V 2021 Nature 592 363-9
- [72] Suchanek T, Kroy K and Loos S A M 2023 Phys. Rev. Lett. 131 258302
- [73] Kreienkamp K L and Klapp S H L 2024 Phys. Rev. Lett. 133 258303
- [74] Berthin R, Fries J D, Jardat M, Dahirel V and Illien P 2025 Phys. Rev. E 111 L023403
- [75] Yiwei Zhang A M and Étienne F 2025 New J. Phys. 27 043023
- [76] Negi R S, Winkler R G and Gompper G 2025 Binary mixtures of intelligent active Brownian particles with visual perception [Data set] Zenodo (https://doi.org/10.5281/zenodo.15208145)